Dalton Transactions

ROYAL SOCIETY OF CHEMISTRY

PAPER

View Article Online
View Journal | View Issue

Cite this: *Dalton Trans.*, 2024, **53**, 4551

Effect of annealing conditions on the luminescence properties and thermometric performance of $Sr_3Al_2O_5Cl_2:Eu^{2+}$ and $SrAl_2O_4:Eu^{2+}$ phosphors

Simon N. Ogugua, *[a] Christopher Abram,[b] Benoît Fond, [c] Robin E. Kroon, [a] Frank Beyrau[d] and Hendrik C. Swart *[a]

We report on the synthesis, photoluminescence optimization and thermometric properties of $Sr_3Al_2O_5Cl_2:Eu^{2+}$ and $SrAl_2O_4:Eu^{2+}$ phosphor powders. The photoluminescence of $Sr_{2.9}Al_2O_5Cl_2:0.1Eu^{2+}$ phosphors exhibits a blue-shift with an increasing annealing temperature owing to a decrease in the crystal field strength of the host caused by evaporation of Cl from the material. The quenching of the blue band in favour of the red band observed in the luminescence spectra of $Sr_{2.9}Al_2O_5Cl_2:0.1Eu^{2+}$ with an increased annealing temperature was explained using the mechanism of the Landau-Zener transitions. The quantum yield and the lifetime of the phosphors depend on the annealing temperature. Phosphor samples annealed at 850 °C, 1000 °C, 1200 °C and 1500 °C were found to be potential luminescence thermometers using the luminescence spectral method. For $Sr_3Al_2O_5Cl_2:Eu^{2+}$ annealed at 1000 °C, the temperature-dependent dual-band intensity ratio demonstrated a high-temperature sensitivity of ~1.47%/°C in the temperature range of 23 °C to 40 °C which is superior to other reported phosphors with a microsecond decay time, suggesting that the material has potential for sensitive thermometry applications at ambient temperatures.

Received 16th November 2023,
Accepted 7th February 2024

DOI: 10.1039/d3dt03836j

rsc.li/dalton

1. Introduction

Temperature is an important parameter in our day-to-day lives. This spans from low-temperature environments of natural processes such as in biological systems[1] and thermal convection in oceans and atmospheres, to high-temperature environments of industrial energy and manufacturing devices such as gas turbines and other reactive systems.[2,3] Knowledge of the temperature is critical. Thermographic phosphors can provide robust solutions for remote temperature measurements. Phosphor thermometry utilizes temperature-sensitive powders which usually consist of host materials doped with small amounts of activator ions like rare-earth and/or transition metal ions.[4] Thermographic phosphors exhibit changes in the luminescence emission intensity, the emission spectrum, or the lifetime with temperature, from which the temperature can be obtained after calibration. The temperature range, sensitivity and precision of measurements are determined by the intrinsic characteristics of the phosphor materials, and it is useful to discover and engineer new materials with enhanced temperature-dependent luminescence properties. To perform temperature measurements, either the temperature dependence of the luminescence decay time or the luminescence emission spectrum is exploited, referred to as the temporal and spectral methods, respectively.[5,6] For two-dimensional measurements, the decay time method requires a camera with the ability to record at least two frames with a short interframe time,[7] while the spectral method requires simultaneously recording two spectrally-filtered images but without specific requirements on the interframe time. Also with the latter method, the measurement time is flexible and can be longer in order to increase the temperature resolution. The spectral method has often been applied on single band phosphors such as ZnO, BAM:Eu, or $(Sr,Mg)(PO_4):Sn^{2+}$,[8–10] the emission band of which broadens and shifts red or blue with temperature, but the resulting temperature sensitivity is typically below 1%/K near room temperature. Dual-band emission from levels in thermal equilibrium are also used, either from single dopant (YAG:Pr^{3+}, MFG:Mn^{4+}, $YVO_4:Dy^{3+}$ (ref. 11–13)) or from

[a]*Department of Physics, University of the Free State, Bloemfontein, ZA9300, South Africa. E-mail: Ogugua.sn@ufs.ac.za, Kroonre@ufs.ac.za, Swarthc@ufs.ac.za*
[b]*Department of Mechanical and Aerospace Engineering, Princeton University, NJ 08544, USA. E-mail: cabram@princeton.edu*
[c]*Department of Aeronautics, ONERA the French Aerospace Lab, 92190 Meudon, France. E-mail: benoit.fond@onera.fr*
[d]*Lehrstuhl für Technische Thermodynamik, Otto-von-Guericke-Universität Magdeburg, 39106 Magdeburg, Germany. E-mail: frank.beyrau@ovgu.de*

co-doping (YAG:Pr^{3+},Ce^{3+}, $Sr_4Al_{14}O_{25}$:Mn^{4+},Tb^{3+}, YAG:Cr^{3+},Er^{3+}, Nd^{3+} (ref. 14–16)). One particularly attractive aspect of the multi-band emission is the possibility to exploit the response with a colour camera, as shown in ref. 15. However, it is difficult to meet both requirements of short decay time of both emission bands for fluid thermometry and high-temperature sensitivity. In this paper, we exploit a dual-band thermometric response from a single dopant, Eu^{2+}, with a decay time on the microsecond scale.

$Sr_3Al_2O_5Cl_2$:Eu^{2+} is generally known for its red-orange or orange-yellow emission and persistent luminescence which lasts for a few seconds. To enhance the afterglow properties of this phosphor, it can be co-doped with rare-earth or post-transition metal ions such as Dy^{3+}, Ce^{3+}, Bi^{3+} and Tm^{3+}.[17–20] Temperature-dependent properties of $Sr_3Al_2O_5Cl_2$:Eu^{2+} have been investigated by Dutczak *et al.*[17] The results show that the emission intensity of the red band of $Sr_3Al_2O_5Cl_2$:Eu^{2+} strongly decreases in the near-ambient temperature range (250 to 350 K). The annealing temperature after the synthesis of $Sr_3Al_2O_5Cl_2$:Eu^{2+} has a significant effect on the PL of the phosphor. When annealed at 850 °C, the phosphor showed two photoluminescence (PL) emission bands around 443 and 600 nm,[21] but when annealed at higher temperatures (1100 °C to 1300 °C) it showed only the 600 nm emission.[17,19,22] Although the luminescence properties and the temperature-dependent luminescence of $Sr_3Al_2O_5Cl_2$:Eu^{2+} has been reported in ref. 21 and 17, the thermometric properties of the material have not been reported, which is the focus of this research.

In this study, we explore the possibility of using $Sr_3Al_2O_5Cl_2$:Eu^{2+} and $SrAl_2O_4$:Eu^{2+} for dual-band and emission band shift thermometry, respectively. $Sr_3Al_2O_5Cl_2$:Eu^{2+} and $SrAl_2O_4$:Eu^{2+} phosphors were synthesised using the solid-state method specifically, with different concentrations of Eu^{2+} and annealing temperatures (850 °C to 1500 °C). We measured the effects of dopant concentration and annealing temperatures on the structure, morphologies, and temperature-dependence of the luminescence, and theoretically explored the potential of these phosphors for remote thermometry using the dual-band and emission band shift approach, with monochrome and colour sensors.

2. Experimental

2.1. Synthesis

Divalent europium doped strontium aluminate chloride ($Sr_{3-x}Al_2O_5Cl_2$:x%Eu^{2+}, x = 0.05, 0.08, 0.1 and 0.15) phosphor particles were prepared by the conventional high-temperature solid-state reaction method. The stoichiometric amount of the starting materials 8.283 mmol of $SrCO_3$ (analytical reagent (A. R.)), 4.141 mmol of $SrCl_2{\cdot}H_2O$ (A. R.), Al_2O_3 (A. R.) and Eu_2O_3 (99.99%) and acetone were used to make a slurry mixture inside a Pyrex borosilicate glass mortar. The mixture was ground using a pestle for about 30 min and annealed using a ceramic crucible in a reducing gas (95% Ar/5% H_2) at 1000 °C for 4 h, allowed to cool to room temperature and the final product was ground for 30 min. A similar process was repeated for other samples, with the concentration of Eu_2O_3 fixed at x = 0.1 for different annealing temperatures, namely 850, 1200 and 1500 °C.

2.2. Characterization

The structure of the samples was analyzed using a Bruker D8 Advance X-ray diffractometer. The morphology studies and the elemental analyses were carried out using a Jeol JSM-7800F field emission scanning electron microscope (FE-SEM) fitted with an Oxford X-MaxN 80 energy-dispersive X-ray spectrometer (EDS). The PL spectra were measured using an FLS980 fluorescence spectrometer (Edinburgh Instruments) equipped with a 450 W xenon lamp as a steady-state excitation source and a Pulsed Light Emitting Diode at 360 nm incorporated in an FLS980 fluorescence spectrometer for lifetime measurements. The quantum yield (QY) measurements were performed using an integrating sphere incorporated in the FLS980 spectrometer. The temperature-dependent PL was measured with a system consisting of a 325 nm He–Cd gas laser excitation source, a spectrometer, a photomultiplier tube detector, and a lock-in amplifier.

3. Results and discussion

3.1. Structure

X-ray diffraction (XRD) patterns of $Sr_{3-x}Al_2O_5Cl_2$:xEu^{2+} (x = 0.05, 0.08, 0.1 and 0.15) annealed at 1000 °C are shown in Fig. 1(a). The samples crystallized as single phase $Sr_3Al_2O_5Cl_2$ consistent with JCPDS file no: 80-0564. The variation in Eu^{2+} concentration did not have a significant effect on the patterns. This is evidence that Eu^{2+} ions are incorporated well in the Sr^{2+} sites, as expected considering their relatively close ionic radii of 1.30 and 1.31 Å, respectively, in their 9-coordinated sites.[23] $Sr_3Al_2O_5Cl_2$ belongs to the $P2_12_12_1$ space group having an orthorhombic crystal structure with three different strontium sites[24,25] as shown in the unit cell in Fig. 1(b). The individual Sr^{2+} site is coordinated by five O^{2-} and four Cl^- ligands (Fig. 1(c)) with differences in the average Sr–O and Sr–Cl bond lengths. In addition, Sr1 and Sr3 form a non-enclosed one-dimensional ring along the [100] plane. Sr2 and Cl are distributed in the large tunnel formed by the Sr1–Sr3 screwed tetrahedron framework.[26] The three Sr sites are linked through AlO_4 tetrahedral matrices.[27]

Images of the morphologies of $Sr_{3-x}Al_2O_5Cl_2$:xEu^{2+} (x = 0.05 and 0.15) phosphors obtained from FE-SEM are shown in Fig. 1(d and e), respectively, showing rod-like structures. Variation in Eu^{2+} content in the samples did not have a significant effect on the morphologies of the phosphors.

Further work focused on a doping concentration of 0.1 mol% which emission intensity was found later in this article (see Fig. 5(b)), to be the highest. Samples with this doping concentration were prepared using different annealing temperatures (850, 1000, 1200 and 1500 °C, represented as

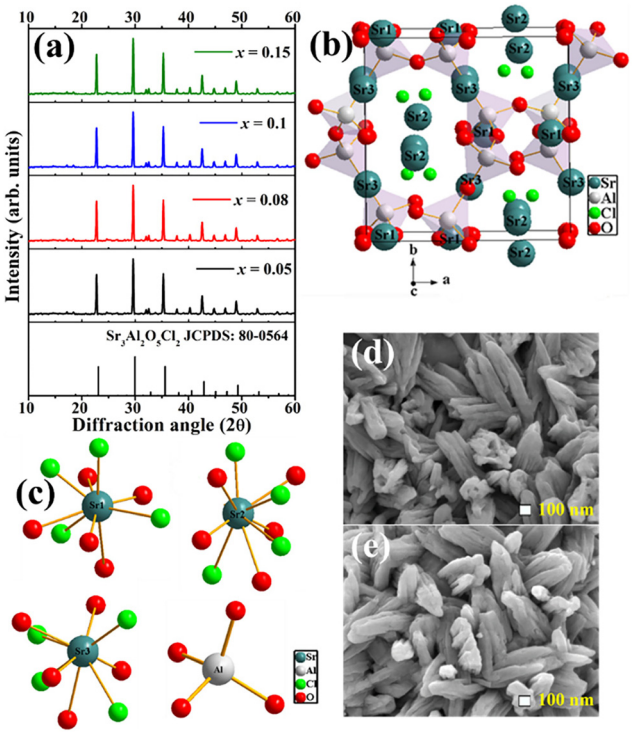

Fig. 1 (a) The XRD patterns of $Sr_{3-x}Al_2O_5Cl_2$:xEu^{2+} (x = 0.05, 0.08, 0.1 and 0.15) phosphors, (b) unit cell of $Sr_3Al_2O_5Cl_2$, (c) the three sites of 9-coordinated Sr^{2+} ions and the tetrahedral Al^{3+} ion, and FE-SEM images for x = (d) 0.05 and (e) 0.15.

SAO:0.1Eu850, SAO:0.1Eu1000, SAO:0.1Eu1200 and SAO:0.1Eu1500, respectively, subsequently) and the XRD patterns are shown in Fig. 2(a). Apart from the crystal planes from $Sr_3Al_2O_5Cl_2$ (JCPDS file no: 80-0564), Fig. 2(b) (enlarged pattern from 15 to 40 2θ) shows that SAO:0.1Eu850 contained some planes from SrO (JCPDS file no: 75-0263) and $SrCl_2$ (JCPDS file no: 77-2165). The presence of SrO and $SrCl_2$ phase is owing to the low annealing temperature. The SAO:0.1Eu1000 and SAO:0.1Eu1200 crystalized as a single phase $Sr_3Al_2O_5Cl_2$ and are consistent with the JCPDS file no: 80-0564. For the higher temperature annealing of 1500 °C, the pattern of the SAO:0.1Eu1500 matched with the JCPDS file no: 74-0794 for $SrAl_2O_4$, indicating the elimination of Cl from the structure. The Rietveld refined results of the SAO:0.1Eu1000 (cell parameters: a = 9.4176 (9) Å, b = 9.3989(6) Å, c = 9.3996(6) Å, and V = 832.05(1) Å^3) and SAO:0.1Eu1200 (cell parameters: a = 9.4064 (5), b = 9.3979(4), c = 9.4233(8) Å, and V = 833.03(8) Å^3), Fig. 2(c and d), revealed that the samples crystallized as an orthorhombic structure with a space group of $P2_12_12_1$. Compared to the standard cell parameters, a = b = c = 9.422 Å, and V = 836.43 Å^3, reported in JCPDS file no: 80-0564, it is seen that the Rietveld parameters showed only a slight reduction. The Rietveld refined result of the SAO:0.1Eu1500, Fig. 2(e) exhibited a monoclinic structure with the $P2_1$ space group belonging to $SrAl_2O_4$. The Rietveld cell parameters: a = 8.4258(7) Å, b = 8.8039(6) Å, c = 5.1497(9) Å, and V = 381.35 Å^3, are in close

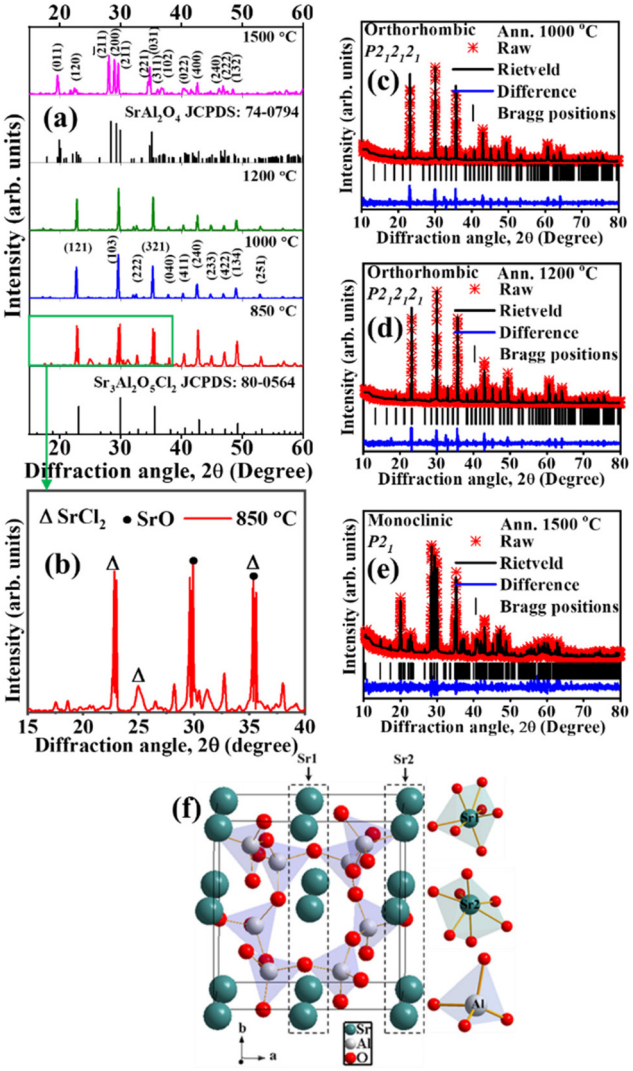

Fig. 2 (a) The XRD patterns of SAO:0.1Eu850, SAO:0.1Eu1000, SAO:0.1Eu1200 and SAO:0.1Eu1500 compared to the standard files; (b) XRD pattern of the SAO:0.1Eu850 showing the diffraction angle range of 20–40 (2θ). Rietveld results of the (c) SAO:0.1Eu1000, (d) SAO:0.1Eu1200, (e) SAO:0.1Eu1500, and (f) the unit cell of the crystal structure of $SrAl_2O_4$.

agreement with the standard cell parameters a = 8.447 Å, b = 8.816 Å, c = 5.163 Å, and V = 383.80 Å^3, reported in JCPDS file no: 74-0794. The crystal structure of $SrAl_2O_4$ contains rings formed by six corners sharing AlO_4 tetrahedra, as displayed in Fig. 2(f). Two non-equivalent strontium sites, Sr1 and Sr2, are situated within the channels formed by the AlO_4 tetrahedra. Both strontium sites are coordinated to seven oxygen ions with average distances of 2.69 Å and 2.67 Å for Sr1 and Sr2, respectively.[28]

3.2. Morphology

FE-SEM micrographs of the SAO:0.1Eu850, SAO:0.1Eu1000, SAO:0.1Eu1200 and SAO:0.1Eu1500 phosphors annealed at different temperatures are shown in Fig. 3. The image of the

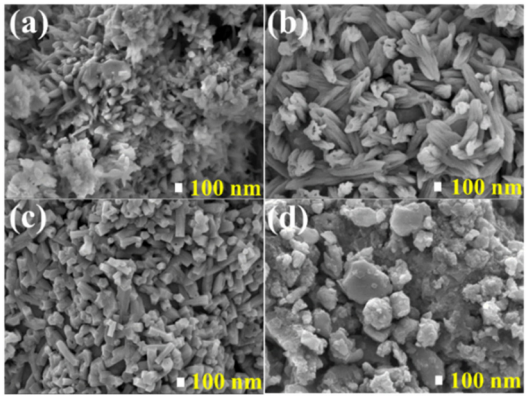

Fig. 3 The FE-SEM images showing the morphologies of the (a) SAO:0.1Eu850, (b) SAO:0.1Eu1000, (c) SAO:0.1Eu1200 and (d) SAO:0.1Eu1500.

SAO:0.1Eu850, Fig. 3(a), exhibited irregular morphology comprising of rod-like, plate-like, and agglomerated structures of different sizes. This is confirmation that the sample consists of mixed phases, as revealed by the XRD result in Fig. 2. In Fig. 3(b and c), the morphology of the SAO:0.1Eu1000 and SAO:0.1Eu1200 exhibited regular rod-like shapes. It is evident from Fig. 3(b and c) that the diameter of the rods reduced, and the shapes became more defined when the sample was annealed at 1200 °C. For the SAO:0.1Eu1500, the particles exhibited different morphology entirely, as shown in Fig. 3(d). The image showed agglomerates of plate-like structures of various sizes.

3.3. Element analysis

Energy dispersive X-ray spectroscopy (EDS) was used for the identification of elements in the samples. The EDS spectra of the SAO:0.1Eu850, SAO:0.1Eu1000 and SAO:0.1Eu1200, shown in Fig. 4 exhibits peaks from Sr, Al, O, C, Cl and Eu, while the spectra of the SAO:0.1Eu1500 contain all these elements except Cl. The absence of Cl suggests that it evaporated completely from the sample at 1500 °C annealing temperature which resulted in the change in the structure and morphologies of the samples as observed in the XRD (Fig. 2(a)) and FE-SEM (Fig. 3(d)) results and is consistent with the XRD identification of $SrAl_2O_4$. The atomic ratios are in good agreement with the compositions identified for annealing at 1000 °C, 1200 °C and 1500 °C (Table 1). Also, note that the elemental composition (Table 1) derived from the EDS spectra (Fig. 4), changed with the increase in the annealing temperature in favour of Al. The decrease in the Sr intensity could be due to a gradual evaporation of the element from the surface of the material as the annealing temperature was increased. This is logical, considering that the boiling point of Sr is 1382 °C and that of Al is 2478 °C. The change in the Al : Sr ratio at a particular annealing temperature adjusts in a manner that maintains charge neutrality at each phase of the material. Jafer *et al.*[29] and Jaffar *et al.*[30] have reported similar phenomena on Y_2O_3:Bi^{3+} and La_2O_3:Bi^{3+}, respectively. In these cases, Bi^{3+} evaporated from the materials at elevated annealing temperatures.

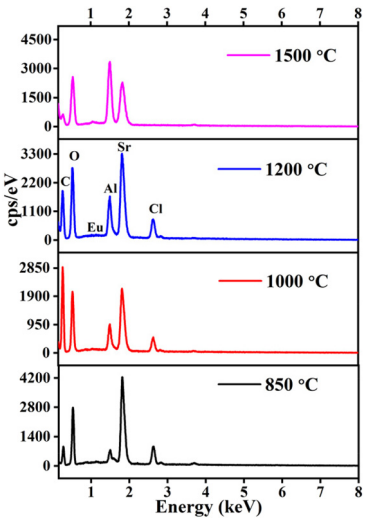

Fig. 4 EDS spectra of SAO:0.1Eu850, SAO:0.1Eu1000, SAO:0.1Eu1200, and SAO:0.1Eu1500.

3.4. Effect of dopant concentration on photoluminescence

The room temperature PL excitation spectra of the $Sr_{3-x}Al_2O_5Cl_2$:xEu^{2+} (x = 0.05, 0.08, 0.1 and 0.15) annealed at 1000 °C when monitoring the 600 nm emission band of Eu^{2+} are shown in Fig. 5(a). The spectra consist of two broad bands stretching from the deep ultraviolet to the near visible range of the electromagnetic spectrum with maxima around 250 and 325 nm. These bands are assigned to the electric-dipole transition from the $^8S_{7/2}$ ground state of the $4f^7$ configuration to the $4f^65d^1$ excited states of Eu^{2+}.[17,21,25] It appears from the excitation spectra that the 250 nm band has higher intensity at a low concentration of Eu^{2+} (x = 0.05 and 0.08), and the 325 nm band showed dominance at a higher Eu^{2+} concentration (x = 0.15). Balance in intensity between these two bands and what appeared to be the best intensity was attained in the sample doped with x = 0.1 of Eu^{2+}.

Fig. 5(b) displays the emission spectra of the phosphors doped with different concentrations of Eu^{2+} excited at 325 nm. The broad bands cover the visible spectrum with maxima at 443 and 600 nm and are assigned to the $4f^65d^1 \rightarrow 4f^7$ electric dipole transitions of Eu^{2+} ions.[21] The origin of the blue and red bands in $Sr_3Al_2O_5Cl_2$:Eu^{2+} is still a topic of discussion. Wang *et al.*[21] published the luminescence of $Sr_3Al_2O_5Cl_2$:Eu^{2+}, Dy^{3+} with emission at 440 nm and 590 nm and assigned the two bands to Eu^{2+} sitting at different sites in the host lattice. In addition, Dutczak *et al.*[17] observed a broad red band with a maximum around 615 nm from $Sr_3Al_2O_5Cl_2$:Eu^{2+},Dy^{3+} and they believe that the broadband originated from overlapping emission bands from Eu^{2+} ions sitting at three different Sr sites (Sr1, Sr2 and Sr3) in the host lattice. The fitted emission spectrum of the sample doped with x = 0.1 of Eu^{2+} (Fig. 5(c)) shows that the broadband with a maximum at 600 nm can be separated into two bands located at 2.10 eV (590 nm) and 2.07 eV (600 nm) and the blue band has a single peak at 2.80 eV

Table 1 Elemental compositions of the materials

Annealing temperature (°C)	Elemental composition (a.u)					Ratios of element to Al		
	Sr	Al	O	Cl	Eu	Sr/Al	Cl/Al	Eu/Al
850	0.47	0.08	1.39	0.23	0.01	5.87	2.88	0.13
1000	0.33	0.18	1.42	0.17	0.01	1.83	0.94	0.06
1200	0.33	0.18	1.45	0.15	0.01	1.83	0.83	0.06
1500	0.36	0.69	1.87	—	0.01	0.52		0.01

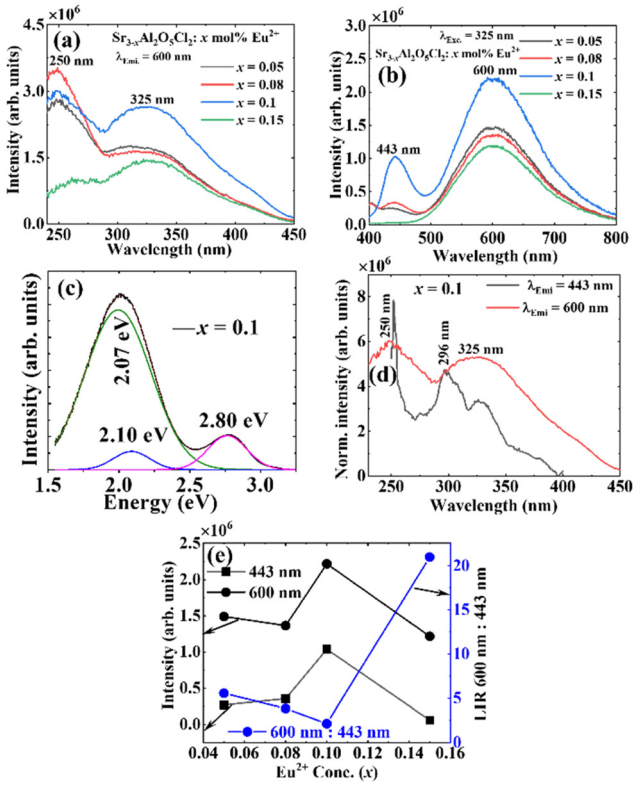

Fig. 5 PL (a) excitation (monitoring 600 nm emission), (b) emission spectra and (c) fitted spectra under 325 nm excitation of $Sr_{3-x}Al_2O_5Cl_2$: xEu^{2+} (x = 0.05, 0.08, 0.1 and 0.15) annealed at 1000 °C. (d) Excitation spectrum of $Sr_{2.9}Al_2O_5Cl_2$:$0.1Eu^{2+}$ under 443 and 600 nm emission. (e) The plot of PL intensity *versus* Eu^{2+} concentration for the 443 nm and 600 nm emission and the luminescence intensity ratio of the 600 nm : 443 nm emission *versus* Eu^{2+} concentration.

(443 nm), which supplements the idea that the emission band is generated from Eu^{2+} occupying different sites in the host lattice. Similar results have been published by Wang *et al.*[21] To further support this view, the excitation spectra of the sample with x = 0.1 recorded at 443 nm and 600 nm emissions were compared in Fig. 5(d). The excitation spectrum recorded at 600 nm emission showed broader band with maximums at 250 and 325 nm, while the one recorded at 443 nm showed narrower band with maximums at 296 and 325 nm. The excitation spectrum under 443 nm emission is assigned to $4f^7 \rightarrow 4f^65d^1$ excitation bands for Eu^{2+} occupying Sr sites with higher coordination numbers (stronger crystal field), whereas the broad spectrum under 600 nm emission contains contributions from $4f^7 \rightarrow 4f^65d^1$ excitation bands of Eu^{2+} occupying all Sr sites, due to partial energy transfer from Eu^{2+} occupying the high energy Sr sites to the red emitting Eu^{2+} ions.[28] Fig. 5(e) shows the plot of the emission intensity *versus* Eu^{2+} concentration for the 443 and 600 nm bands, with the sample doped with x = 0.1 Eu^{2+} having the highest intensity in both bands. It is also evident from Fig. 5(e) that the luminescence intensity ratio (LIR) of the 443 nm bands with respect to the 600 nm bands increased with Eu^{2+} concentration and attained a maximum when x = 0.1 and quenched completely when x = 0.15. The latter phenomenon could be due to energy transfer among Eu^{2+} ions occupying different Sr sites in the host lattice.

3.5. Effect of annealing on photoluminescence

The normalized room temperature PL excitation spectra of the SAO:0.1Eu850, SAO:0.1Eu1000, SAO:0.1Eu1200 and SAO:0.1Eu1500 when monitoring the 600 nm emission bands are shown in Fig. 6(a). The spectra extended from the ultraviolet region to the visible wavelength with maxima at 250 and 325 nm, showing similar features as the spectra shown in

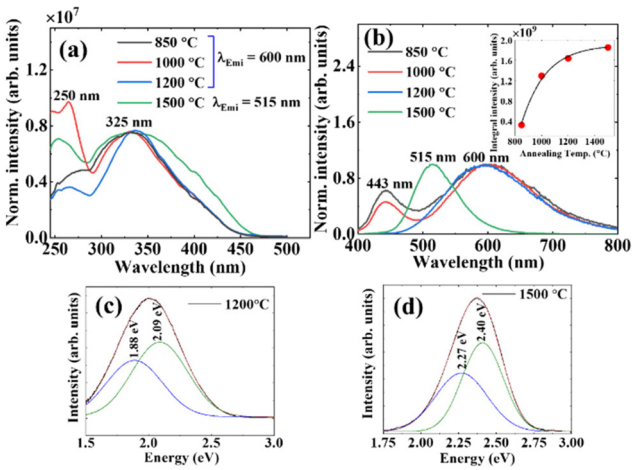

Fig. 6 (a) Normalized room temperature PL excitation spectra of SAO:0.1Eu850, SAO:0.1Eu1000, SAO:0.1Eu1200, and SAO:0.1Eu1500. (b) Normalized room temperature PL emission spectra of SAO:0.1Eu850, SAO:0.1Eu1000, SAO:0.1Eu1200 and SAO:0.1Eu1500. The inset of (b) is the plot of the emission intensities as a function of the annealing temperatures. Fitted PL spectra of the (c) SAO:0.1Eu1200 and (d) SAO:0.1Eu1500.

Fig. 5(a). However, the spectrum of the SAO:0.1Eu1500 broadened towards a higher wavelength compared to the rest.

The normalized room temperature PL emission spectra of SAO:0.1Eu850, SAO:0.1Eu1000, SAO:0.1Eu1200, and SAO:0.1Eu1500 (measured at 325 nm excitation) exhibited broad bands which displayed different features in the visible wavelength region as shown in Fig. 6(b). The SAO:0.1Eu850 shared similar features with the SAO:0.1Eu1000, showing a blue and red band with maxima at 443 nm and 600 nm, respectively.

The SAO:0.1Eu1200 showed a similar PL emission band at 600 nm, but the 443 nm band was quenched completely. The SAO:0.1Eu1500 exhibited greenish emission with a maximum at 520 nm, which is characteristic of $SrAl_2O_4$:Eu^{2+}.[28] Note that the emission spectra reduced from dual to single-band for annealing temperatures over 1000 °C. The plot of the integrated emission intensity of the phosphors *versus* the annealing temperatures (inset of Fig. 6(b)) shows almost a logarithmic regression. This makes sense since the sample annealed at 850 °C is only partially the target phase. The fitted PL spectra of the SAO:0.1Eu1200 and SAO:0.1Eu1500, Fig. 6(c and d) shows two bands each at 1.88 eV (660 nm) and 2.09 eV (593 nm), and 2.27 eV (546 nm) and 2.40 eV (517 nm), respectively. The two bands observed from the fitted PL spectrum of the SAO:0.1Eu1500 is assigned to the two Sr sites (Sr1 and Sr2) in $SrAl_2O_4$ as shown in the crystal structure in Fig. 2(e).

The mechanism behind the quenching of the blue band in the SAO:0.1Eu1200 has not been fully understood. Nevertheless, using other features observed in the emission spectra and the results from different techniques, the underlying mechanism of the quenching can be explained. In Fig. 6(b), there is a slight blue broadening of the 600 nm emission band as the annealing temperature was increased. A similar phenomenon has been reported for Eu^{2+} doped in host lattices such as $BaMgAl_{10}O_{17}$ and $SrMgAl_{10}O_{17}$,[31] $BaCN_2$,[32] Ca_2SiO_4 and $NaBaPO_4$ [33] when the luminescence of the phosphors was measured at different temperatures, and it was assigned to reduced lattice vibration,[31,34] which leads to a decrease in crystal field strength of the lattice.[35] Dutczak *et al.*[17] reported a similar phenomenon in $Sr_3Al_2O_5Cl_2$:Eu^{2+} and attributed it to the blue-shift in the emission spectrum due to faster quenching of the red emission. However, they excluded the possibility of inter-site energy transfer between Eu^{2+} ions. The quenching of the blue band has been widely studied in $SrAl_2O_4$:Eu^{2+}, and there is a general agreement that it is due to the thermal activated non-radiative energy transfer between Eu^{2+} ions occupying different Sr sites in the host lattice.[36,37] However, instead of the blue-shift as observed in $Sr_3Al_2O_5Cl_2$:Eu^{2+}, a red-shift was observed in $SrAl_2O_4$:Eu^{2+}, which suggests that the splitting of the 5d state of the Eu^{2+} ions is due to the increase in the crystal field strength of the lattice which results to the reduction in the energy between the $4f^65d^1$ and $4f^7$ states.[38] The sample annealed at a very high temperature (1500 °C) changed from $Sr_3Al_2O_5Cl_2$:Eu^{2+} to $SrAl_2O_4$:Eu^{2+}, as confirmed by the XRD, EDS, and PL results. This is due to the evaporation of Cl in the material during synthesis as the annealing temperature increases. As seen from the EDS spectra (see Fig. 4), the Cl peak totally disappeared from the spectrum of the SAO:0.1Eu1500. The gradual evaporation of Cl from the material probably will result in a decrease in the crystal field strength of the host which leads to the blue-shift observed in the PL as the annealing temperature was increased in Fig. 6(b). Indeed, the ratio of Cl to Al and Sr is lower for the sample annealed at 1200 °C than the one annealed at 1000 °C. Furthermore, considering the SAO:0.1Eu850, SAO:0.1Eu1000 and SAO:0.1Eu1200, the higher the annealing temperature, the more crystalline they become. This strongly influenced the PL characteristics since lanthanide ions in a host with higher crystallinity experience a stronger crystal field.[39,40] Therefore, at a higher temperature, the system will try to attain equilibrium between the decreasing crystal field strength due to the Cl vacancies and the increasing crystal field strength due to the improved crystallinity of the material. At the point of equilibrium in the system, there could be energy transfer from the Eu^{2+} occupying the Sr1 site in the host to the Eu^{2+} occupying the Sr2 site through Landau-Zener transitions[36,41] as illustrated in Fig. 7. It is well known that the energy level difference between the $4f^65d^1$ and $4f^7$ states for divalent and trivalent rare earth ions decreases with increase in the crystal field strength of a host.[42,43] The reduction in energy difference between the ground state and the first excited state will cause efficient energy transfer between the Eu^{2+} ions occupying different sites in the host lattice, hence quenching the higher energy luminescence centers.[44,45]

Fig. 7 illustrates the energy configuration diagram of the system as a function of configuration coordinate, q, according to the fitted PL spectrum in Fig. 5(c). The ground state ($4f^7$ level) is made up of a parabola and the excited states ($4f^65d^1$ level) are made up of three parabolas representing the energy levels of the Eu^{2+} ions occupying the Sr1 (443 nm), Sr2 (590 nm) and Sr3 (600 nm) sites (represented as Sr1, Sr2 and

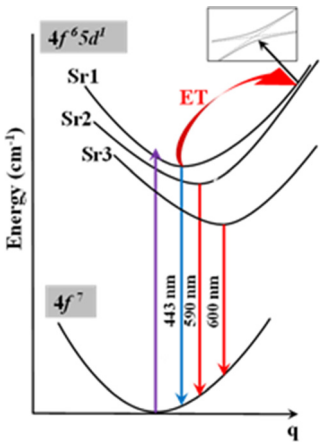

Fig. 7 Schematic configuration diagram of the energy E as a function configuration coordinate q, explaining the energy transfer from Eu^{2+} ions occupying Sr1 to Eu^{2+} ions occupying Sr2 through Landau-Zener transitions.

Sr3 levels henceforth) in the matrix. The Sr1 and Sr2 levels demonstrate the avoided crossing phenomenon (the inset of Fig. 7 illustrates the probability of diabatic transition between the two energy levels). In this model, once excited, electrons will populate the three sites. For the sample annealed at 850 °C and 1000 °C, the three sites can contribute to the emission. At higher annealing temperature, when the system has attained equilibrium in crystal field strength, the energy difference between the Sr1 and Sr2 levels would be minimal, and due to the electron-vibrational coupling and interaction between the Eu^{2+} ions occupying these sites, energy could be transferred non-radiatively from Sr1 to Sr2. The closer the energy gap between Sr1 and Sr2 levels, the more energy will be transferred from Sr1 to Sr2 site until the emission from the Sr1 site is quenched completely. This energy transfer from the Sr1 to Sr2 site explains why the intensity and the area covered by the emission from the Sr2 site increased in Fig. 6(c) when compared to that of Fig. 5(c). Additionally, the red-shift in the peak positions in Fig. 6(c) compared to the peak positions in the fitted red band in Fig. 5(c) can be explained by increased crystal field strength as the phosphor crystallinity increases.

3.6. Lifetime

The fitted decay curves of SAO:0.1Eu850, SAO:0.1Eu1000, and SAO:0.1Eu1200, (monitoring the emission at 600 nm) and SAO:0.1Eu1500 (monitoring the emission at 515 nm) are shown in Fig. 8(a). Also, the fitted decay curves of the 443 nm band of SAO:0.1Eu850 and SAO:0.1Eu1000 are shown in Fig. 8(b).

In both cases, the lifetimes were excited using an LED 360 nm incorporated in the FLS980 fluorescence spectrometer.

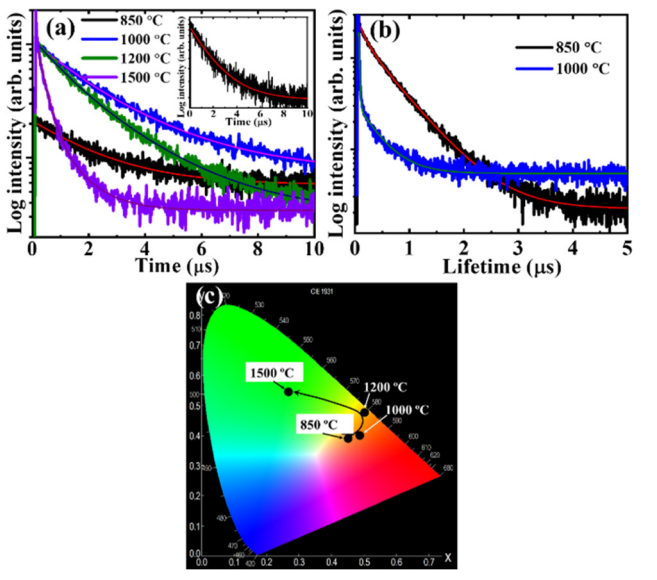

Fig. 8 The decay curves of the (a) 600 nm and (b) 443 bands, and (c) CIE coordinates of the SAO:0.1Eu850, SAO:0.1Eu1000, SAO:0.1Eu1200, and SAO:0.1Eu1500; the inset of (a) is the enlarged decay curve for the SAO:0.1Eu850.

For a material with an N^{th} order exponential decay and luminescent intensity $I(t)$ at time 't', the decay curve can be represented by eqn (1) as

$$I(t) = \sum_{i=1}^{N} A_i \exp\left(-\frac{t}{\tau_i}\right) \quad (1)$$

where A_i and τ_i are the amplitudes and decay times of the N^{th} exponential components of the luminescence decay respectively.[46] The SAO:0.1Eu850 (magnified curve in the inset of Fig. 8(a)) was well fitted by a single exponential equation, while the SAO:0.1Eu1000, SAO:0.1Eu1200 and SAO:0.1Eu1500 were fitted by double exponential equations. The average decay time τ^* for a double exponential curve is defined by eqn (2),

$$\tau^* = \frac{A_1\tau_1^2 + A_2\tau_2^2}{A_1\tau_1 + A_2\tau_2} \quad (2)$$

The fitted first and second components of the lifetimes and the calculated average lifetimes of the SAO:0.1Eu850, SAO:0.1Eu1000, SAO:0.1Eu1200, and SAO:0.1Eu1500 are shown in Table 2. The average lifetime showed annealing temperature-dependent behaviour, with the SAO:0.1Eu1500 having a lifetime significantly shorter (0.6 μs) than the SAO:0.1Eu 1000 (>2.5 μs). For the 443 nm band, the lifetime of SAO:0.1Eu850 has a value twice that of SAO:0.1Eu1000. The reduction in the lifetime could be ascribed to a change in the multiphonon relaxation rate due to a change in the elemental composition of the host materials at different annealing temperatures.

The changes observed in the luminescence spectra of the SAO:0.1Eu850, SAO:0.1Eu1000, SAO:0.1Eu1200, and SAO:0.1Eu1500 (see Fig. 6(b)) are evident in the tunable colours shown in the CIE coordinates in Fig. 8(c). The (x, y) components of the CIE coordinates of the SAO:0.1Eu850, SAO:0.1Eu1000, SAO:0.1Eu1200, and SAO:0.1Eu1500 are shown in Table 3. The emitted colours of the samples are tuned from red, through yellow to green as the annealing temperature was increased.

The quantum yield (QY) of the samples was measured using an integrating sphere incorporated in the FLS980 spectrometer and the results are tabulated in Table 3. A detailed setup for the QY was discussed in our previous work.[47] The QY increased with annealing temperature from 28% to 35%, for the SAO:0.1Eu850 and SAO:0.1Eu1000, respectively, and decreased to 27% for the SAO:0.1Eu1200 and SAO:0.1Eu1500.

3.7. Temperature-dependent luminescence

The temperature-dependent PL spectra of the SAO:0.1Eu850, SAO:0.1Eu1000, SAO:0.1Eu1200, and SAO:0.1Eu1500 were recorded using a 325 nm He–Cd laser system and the results are shown in Fig. 9. The PL intensity displayed a quenching of the red emission band in the measurement range of 26 °C to 100 °C for SAO:0.1Eu850, SAO:0.1Eu1000 and SAO:0.1Eu1200, and the green band for SAO:0.1Eu1500. This quenching is more pronounced for the low annealing temperature

Table 2 The fitted lifetime components and the calculated average lifetimes of the SAO:0.1Eu850, SAO:0.1Eu1000, SAO:0.1Eu1200, and SAO:0.1Eu1500 excited using an LED 360 nm

Annealing temperatures (°C)	$\lambda_{Emi.}$ (nm)	τ_1 (μs)	τ_2 (μs)	τ^* (μs)	$\lambda_{Emi.}$ (nm)	τ_1 (μs)	τ_2 (μs)	τ^* (μs)
850	600	2.1	—	2.1	443	0.2	0.6	0.6
1000	600	1.2	2.8	2.5	443	0.04	0.4	0.3
1200	600	1.0	2.4	2.0	—	—	—	—
1500	515	0.3	1.0	0.6	—	—	—	—

Table 3 CIE (x, y) coordinates and the QY of the SAO:0.1Eu850, SAO:0.1Eu1000, SAO:0.1Eu1200, and SAO:0.1Eu1500

Annealing temperatures (°C)	CIE coordinates (x, y)	QY (%)
850	(0.477, 0.403)	28
1000	(0.484, 0.412)	35
1200	(0.518, 0.457)	27
1500	(0.289, 0.564)	27

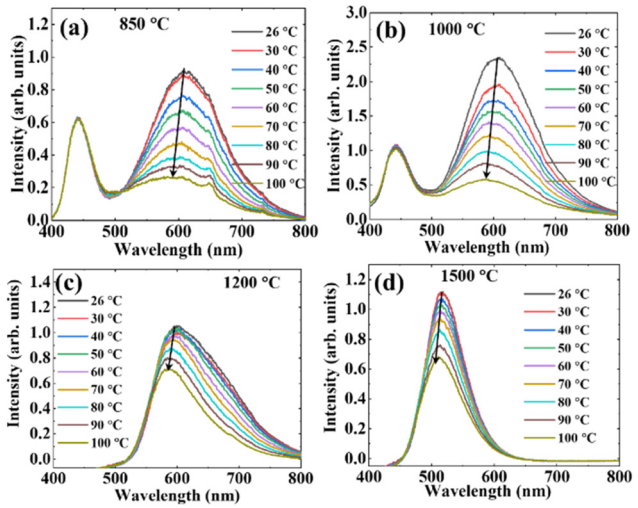

Fig. 9 Temperature-dependent photoluminescence spectra of the (a) SAO:0.1Eu850, (b) SAO:0.1Eu1000, (c) SAO:0.1Eu1200, and (d) SAO:0.1Eu1500 excited using a 325 nm Cd–He laser.

(<1200 °C) samples than for the 1200 °C and 1500 °C samples. The blue emission band, which is only found in the low annealing temperature samples, is unaffected by quenching, which offers a suitable reference for ratiometric measurements. With regards to the shape of the red emission band, the SAO:0.1Eu1200 shows a pronounced shift and broadening of the band which is much less pronounced in the other samples.

In all cases, the broad red emission bands are assigned to the $4f^65d^1 \rightarrow 4f^7$ electric dipole transitions of Eu^{2+} ions.[21] The shape of the emission bands of the SAO:0.1Eu850 suggests the presence of some Eu^{3+} emission lines around 648 nm and 730 nm, which are assigned to the $^5D_0 \rightarrow {}^7F_3$ and $^5D_0 \rightarrow {}^7F_5$ transitions, respectively.[48,49] The mechanism behind the blue-shift observed mainly in the SAO:0.1Eu1200 from red to green (600–586 nm) could be due to the decrease in the crystal field of the host around the Eu^{2+} ions, as explained earlier.

The values of the full width at half maximum (FWHM) of the red emission band (green band for SAO:0.1Eu1500) increased with increasing temperature for all samples but are much more pronounced for the SAO:0.1Eu1200, as shown in Fig. 10(a). This phenomenon has been reported in different phosphor materials[8,9,31,32,34,50–52] and can be attributed to the reduced lattice vibration on decreasing the temperature[31,34,50] due to the temperature dependence of the electron–phonon interaction.[51]

The phenomena underlying a usable luminescence thermometry response of the phosphor materials include the temperature quenching of luminescence when the temperature of a material is increased,[53] temperature-dependent blue or red shift of emission position and[9] back energy transfer between two states.[54] The temperature quenching effect can be explained using the Mott–Seitz theory.[53] Here, the temperature-dependent luminescence spectrum of the SAO:0.1Eu1000 (Fig. 9(b)) is used as an example, and the underlying mecha-

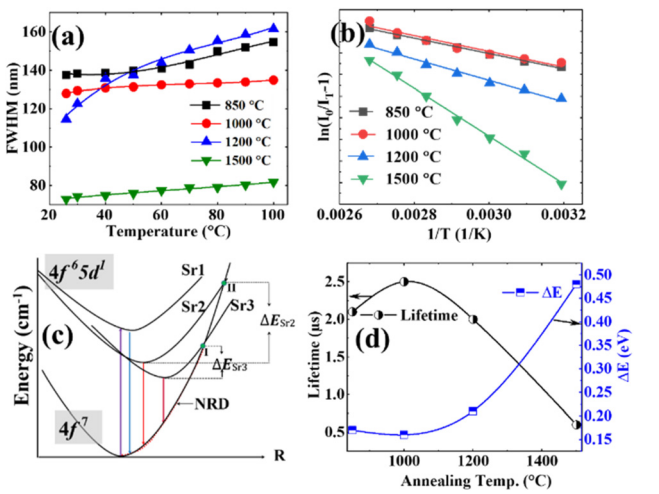

Fig. 10 (a) The FWHM of the emission spectra of the phosphors annealed at different temperatures as a function of the measurement temperature, (b) the plot of emission intensity *versus* temperature, for the red emission band (green band for SAO:0.1Eu1500) (c) the configuration coordinate diagram illustrating the energy levels and thermal quenching mechanism of Eu^{2+} ions occupying the Sr1, Sr2 and Sr3 sites relative to the $4f^7$ ground state for the SAO:0.1Eu1000 and (d) room temperature decay time and estimated values of ΔE for the various annealing temperatures.

nism is illustrated using a configuration coordinate model consisting of four parabolas representing the $4f^7$ ground state of Eu^{2+}, and the Eu^{2+} ions occupying the Sr1, Sr2 and the Sr3 sites in the $4f^65d^1$ excited state, Fig. 10(c). According to this model, an electron in the Sr1 site, assisted by thermal energy, non-radiatively deexcites to the $4f^7$ ground state through the intersection I of the Sr1 and $4f^7$ parabolas[53,55] with the temperature-dependent rate described by eqn (3):[15]

$$\frac{-\Delta E}{k_B}\cdot\frac{1}{T}=\ln\left(\frac{I_0}{I_T}-1\right) \quad (3)$$

where $\Delta E = \Delta E_{Sr_3} + \Delta E_{Sr_2}$ is the sum of the energy difference between the bottom of the Sr3 and Sr2 parabola and I and II, respectively, k_B is a Boltzmann constant, I_0 and I_T are the initial emission intensity (in this case at T = 26 °C) and emission intensity at any given temperature T, respectively. The ΔE was obtained by taking the emission intensity from 500 to 800 nm for the SAO:0.1Eu850 and SAO:0.1Eu1000, and 400 to 800 nm for the SAO:0.1Eu1200, SAO:0.1Eu1500and plotting the $\ln(I_0/I-1)$ *versus* the inverse of temperature (Fig. 10(b)). The values of the ΔE for the SAO:0.1Eu850, SAO:0.1Eu1000, SAO:0.1Eu1200, and SAO:0.1Eu1500 are $\Delta E \approx 0.17$, $\Delta E \approx 0.16$ eV, $\Delta E \approx 0.21$ eV, and $\Delta E \approx 0.48$ eV respectively. The non-radiative deexcitation (NRD) rate at room temperature is higher for smaller ΔE and increases with temperature increase; therefore, the NRD rate follows the order SAO:0.1Eu1000 > SAO:0.1Eu850 > SAO:0.1Eu1200 > SAO:0.1Eu1500. Since the radiative lifetime of a material decreases with the NRD rate,[56] and a lower value of ΔE results in an increase in the NRD rate at room temperature, it implies that the lifetime will decrease with increasing ΔE and *vice versa*. The measured lifetime of the 600 and 515 nm bands and estimated ΔE are plotted as a function of annealing temperature in Fig. 10(d) and support this interpretation.

The temperature-sensitive nature of the emission spectra of the SAO:0.1Eu850, SAO:0.1Eu1000, SAO:0.1Eu1200 and SAO:0.1Eu1500 phosphor powders suggests that the materials have potential for thermometric applications. Thermometric parameters for the LIR technique were derived. For the SAO:0.1Eu850 and SAO:0.1Eu1000, the two-band approach was applied to the temperature-dependent luminescence data (Fig. 9(a and b)) by taking the LIR of the red band (500–800 nm) to the blue band (400–500 nm) defined as band 2 and band 1, respectively. In this case, the LIR is defined by eqn (4) (ref. 6, 57 and 58) as

$$\mathrm{LIR}_{\text{band 2:band 1}}=\frac{I_{\text{band 2}}}{I_{\text{band 1}}} \quad (4)$$

where $I_{\text{band 2}} = I_{500-800}$ is the emission intensity from 500–800 nm and $I_{\text{band 1}} = I_{400-500}$ is the emission intensity from 400–500 nm. For the SAO:0.1Eu1200 and SAO:0.1Eu1500, an emission band shift approach was considered to exploit the temperature-dependent luminescence data (Fig. 9(c)) by taking the LIR of the spectral regions (λ2 and λ1) of 560–800 nm to 470–560 nm and 485–800 nm to 420–485 nm, respectively. Using eqn (5), the LIR can be determined according to ref. 59–61.

$$\mathrm{LIR}_{\lambda 2:\lambda 1}=\frac{I_{\lambda 2}}{I_{\lambda 1}} \quad (5)$$

where $I_{\lambda 2}$ and $I_{\lambda 1}$ are the emission intensity from 560–800 nm to 470–560 nm, respectively, using the temperature-luminescence spectra of SAO:0.1Eu1200 as an example. The wavelength ranges for band 1 and band 2, and λ_1 and λ_2 used for the LIR of the different phosphors are listed in Table 4.

The LIR obtained from the temperature-dependent luminescence emission spectra of the SAO:0.1Eu850, SAO:0.1Eu1000, SAO:0.1Eu1200 and SAO:0.1Eu1500 (Fig. 9(a–c)) decreased monotonically with temperature as shown in Fig. 11(a). The LIR of the temperature-dependent luminescence was fitted using a cubic polynomial function given by eqn (6) and plotted in Fig. 11(a).

$$A+BT+CT^2+DT^3 \quad (6)$$

where A, B, C and D are fitting parameters of polynomial, and T is temperature.

The absolute and relative sensitivities S_a and S_r are defined by eqn (7) and (8) as

$$S_a=\left|\frac{\mathrm{d(LIR)}}{\mathrm{d}(T)}\right| \quad (7)$$

$$S_r=\left|\frac{1}{\mathrm{LIR}}\frac{\mathrm{d(LIR)}}{\mathrm{d}(T)}\right|\times 100\% \quad (8)$$

where d(LIR) is the change in the LIR relative to the change in temperature, d(T). The sensitivities were calculated from the fitted LIR data. The S_a and S_r obtained from the LIR of the SAO:0.1Eu850, SAO:0.1Eu1000, SAO:0.1Eu1200 and SAO:0.1Eu1500 were plotted as a function of temperature as presented in Fig. 11(b) and (c). The S_r value of the SAO:0.1Eu850 increased monotonically with temperature from 1.08%/°C at 26 °C and attained a maximum value of 1.75%/°C at 75 °C and started to decrease. Contrastingly, the S_a value of SAO:0.1Eu850 maintained a constant maximum value of 0.047 $°C^{-1}$ from 26 to 42 °C and began to decrease with increasing temperature. For the SAO:0.1Eu1000, S_r decreased from 1.58%/°C at 26 °C to 1.08%/°C at 60 °C and started to increase, while S_a attained a maximum value of 0.078 $°C^{-1}$ at 26 °C. It is evident that SAO:0.1Eu1000 has a better thermal sensitivity from 26 °C to 40 °C and from 84 °C to 100 °C, while

Table 4 Wavelength ranges for band 1 and band 2, and, and λ_1 and λ_2

Phosphors	Band 1 (nm)	Band 2 (nm)	$I_{\text{band 1}}$	$I_{\text{band 2}}$
SAO:0.1Eu850	400–500	500–800	$I_{400-500}$	$I_{500-800}$
SAO:0.1Eu1000	400–500	500–800	$I_{400-500}$	$I_{500-800}$
	λ1 (nm)	λ2 (nm)	$I_{\lambda 1}$	$I_{\lambda 2}$
SAO:0.1Eu1200	470–560	560–800	$I_{470-500}$	$I_{560-800}$
SAO:0.1Eu1500	420–485	485–800	$I_{420-500}$	$I_{485-800}$

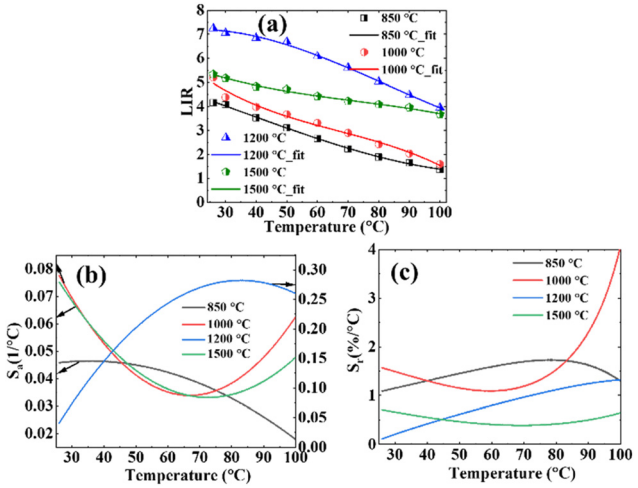

Fig. 11 (a) LIR, (b) S_a and (c) S_r as a function of temperature for the SAO:0.1Eu850, SAO:0.1Eu1000, SAO:0.1Eu1200 and SAO:0.1Eu1500.

the SAO:0.1Eu850 showed better relative thermal sensitivity across 37 °C to 84 °C. Although the SAO:0.1Eu1000 has better sensitivity around room temperature, the SAO:0.1Eu850 offers the best overall thermal response as defined in ref. 62, since its ratio is closer to unity, but the SAO:0.1Eu1000 has the highest quantum yield; therefore, both luminescence thermometers are expected to have a similar overall performance. On the other hand, both SAO:0.1Eu1200 and SAO:0.1Eu1500 have a lower relative temperature sensitivity over the entire range than the samples annealed at lower temperatures. For the SAO:0.1Eu1200, S_r values of 0.12 and 1.32%/°C were obtained at 26 °C and 100 °C, respectively. In comparison, the SAO:0.1Eu1500 has the S_r values of 0.71 and 0.65%/°C at 26 °C and 100 °C, respectively. However, SAO:0.1Eu1200 has the best overall S_a value of 0.102 to 0.282 $°C^{-1}$ from 33 °C to 83 °C, respectively.

The colour response of the four phosphors is shown in Fig. 12(a–d). SAO:0.1Eu1000 has the most pronounced colour response, followed by SAO:0.1Eu850. This colour response is well suited for temperature imaging with a colour camera, *e.g.*, ref. 15. As a thermometric parameter we determined the relative sensitivities of the colour coordinates x, and y, as in ref. 15. It was found to be as high as 0.88%/°C and 1.0%/°C at 90 °C from SAO:0.1Eu1000, which is higher than $Sr_4Al_{14}O_{25}$:Mn^{4+},Tb^{3+} used with a colour camera in ref. 15. The colour response of SAO:0.1Eu1200 and SAO:0.1Eu1500 are comparatively far less pronounced. In the absence of a reference band, their thermometric performance as a luminescence thermometer is expected to be worse than the two other samples.

Furthermore, all the samples exhibited excellent thermometric reproducibility during multiple heating–cooling cycles between 26 to 100 C, as shown in Fig. 13(a–d). This is evidence that the thermometric properties of these materials are sustainable in this temperature range.

The thermometric performances of the phosphors at different temperature ranges and 30 °C and their room temperature lifetimes are compared to earlier reported phosphors in Table 5. The maximum value of the relative sensitivity ($S_{r,max}$) of SAO:0.1Eu1000 is among the best-reported values. Also, only a few phosphors have better S_r value at 30 °C than this phosphor, but they involved either a very long band

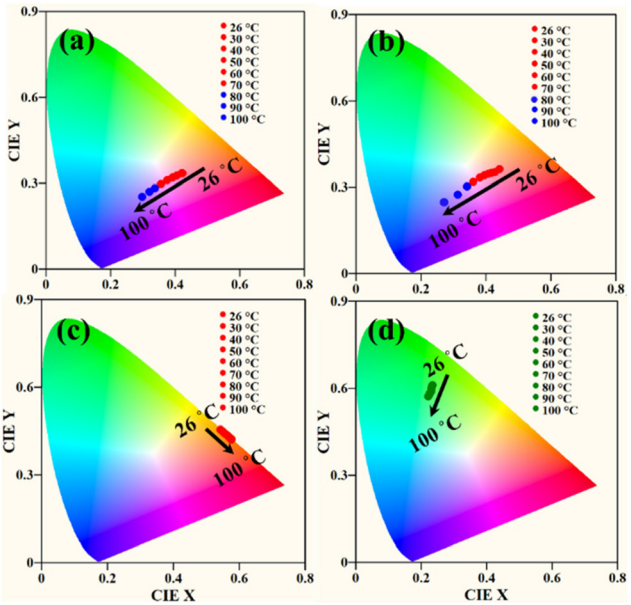

Fig. 12 The CIE coordinates showing the colour response of the (a) SAO:0.1Eu850, (b) SAO:0.1Eu1000, (c) SAO:0.1Eu1200 and (d) SAO:0.1Eu1500.

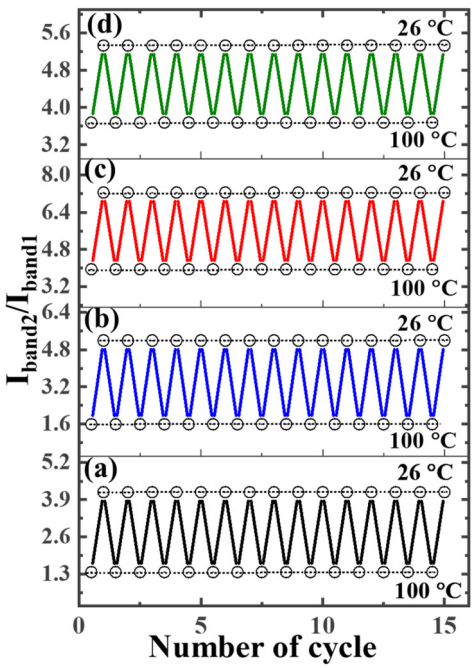

Fig. 13 Repeatability heating–cooling cycles between 26 and 100 °C For (a) SAO:0.1Eu850, (b) SAO:0.1Eu1000, (c) SAO:0.1Eu1200 and (d) SAO:0.1Eu1500.

Table 5 The ratiometric luminescence relative thermal sensitivity (S_r) of different thermometric phosphors and their lifetimes at room temperature

Phosphor	S_r, max%/°C	$T(S_r, \max)$ °C	S_r@30 °C	Tau (S_r, max)	$\lambda_{Exc.}$ (nm)	Ref.
ZnO	2.00	227	0.75	700 ps	355	8
BAM:Eu^{2+}	0.25	22	0.23	1.17 μs	355	8 and 63
$Sr_4Al_{14}O_{25}$:Mn^{4+},Tb^{3+}	2.8	150	0.42	2.1, 2.1 (ms)	266	15
YVO_4:Dy^{3+}	1.8	25	1.6	140 (μs)	310	13
$NaYF_4$:Er^{3+},Yb^{3+}	1.20	27	—	—	980	64
$Ca_6BaP_4O_{17}$:Eu^{2+}	1.53	227	0.25	2.1 (μs)	300	65
$Na_3Sc_2P_3O_{12}$:Eu^{2+},Mn^{2+}	1.56	200	0.42	364.27 (ns), 16.83 (ms)	340	66
$LaAlO_3$:Eu^{2+},Eu^{3+}	1.19	130	0.39	482.68 (ns), 1.64 (ms)	360	67
$Li_4SrCaSi_2O_4N_{8/3}$:Eu^{2+}	1.76	200	0.15	178.3, 269.8 (ns)	363	68
$Sr_4Al_{14}O_{25}$:Eu^{2+}	0.62	100	0.05	34.41, 657.27 (ns)	290	69
$Sr_4La(PO_4)_3OEu^{2+}$,Sm^{3+}	0.48	300	0.15	326.00 (ns), –	412	70
$Ca_8Mg_3Al_2Si_7O_{28}$:Ce^{3+},Eu^{2+}	1.35	227	0.52	30.10, 890.00 (ns)	320	71
$CsPbBr_3/EuPO_4$	1.80	177	0.20	—	393	72
$Ba_5SiO_4Cl_6$:Eu^{2+}	0.87	225	0.07	10.50, 9.60 (μs)	397	73
$La_5Si_2BO_{13}$:Ce^{3+},Eu^{2+}	3.22	20	3.00	13.85 (ns), —	345	74
$CsCu_2I_3$:Eu^{2+}	2.60	−13	1.95	1.66.00 (μs), 87.04 (ns)	310	75
$La_{0.17}Gd_{0.8}AlO_3$:Eu^{2+},Eu^{3+}	3.23	30	3.23	352.80 (ns), 1.63 (ms)	315	76
$MgAl_2O_4$:Eu^{2+},Eu^{3+}	0.83	200	0.26	2.12 (μs), 1.26 (ms)	358	77
$Ca_9Zn_{1.5}(PO_4)_7$:Eu^{2+},Eu^{3+}	1.40	180	0.14	258.72 (ns), 0.68 (ms)	362	78
$SrAl_2Si_2O_8$:Eu^{2+},Eu^{3+}	0.22	300	0.01	5.80 (μs), 1.87 (ms)	324	79
$Sr_{2.94}Eu_{0.01}La_{1.05}P_{2.95}Si_{0.05}O_{12}$	1.30	30	1.30	220.43, 429.10 (ns)	375	80
$Ca_2Al_2SiO_7$:Eu^{2+},Eu^{3+}	2.46	170	1.35	210.30 (ns), 2.25 (ms)	394	81
$LiSr_4(BO_3)_3$:Ce^{3+},Eu^{2+}	4.02	20	3.80	12.6 (ns), 286.10 (ns)	356	82
SAO:0.1Eu800	1.75	75	1.16	0.6, 2.1 (μs)	325	This work
SAO:0.1Eu1000	4.00	100	1.49	0.3, 2.5 (μs)	325	This work
SAO:0.1Eu1200	1.32	100	0.21	2.0 (μs)	325	This work
SAO:0.1Eu1500	0.65	100	0.67	0.6 (μs)	325	This work

Row with a pair of lifetimes represents the lifetimes of the two dopant ions, respectively, or in the case of a single dopant, the lifetime at two emission wavelengths.

>100 μs (*e.g.*, the emission for Eu^{3+} (ref. 76 and 81) or Dy^{3+} (ref. 53)) or a very short band <10 ns (emission from Ce^{3+} (ref. 74) or a charge transfer band[75]). Here, the decay time of both bands is in the microsecond range, which is ideally suited for imaging fast moving objects, *e.g.*, gas and liquid flows using phosphor particles as tracers, and also for time-gated imaging in applications where fluorescence must be avoided.[83] In summary, $Sr_3Al_2O_5Cl_2$:Eu^{2+} is an excellent candidate phosphor for sensitive dual-band thermometry at ambient temperatures where lifetimes in the microsecond range are required.

4. Conclusion

$Sr_3Al_2O_5Cl_2$:Eu^{2+} and $SrAl_2O_4$:Eu^{2+} thermographic phosphor particles were prepared and demonstrated to be highly sensitive to temperature in the ambient region. The optimal emission was obtained from the sample doped with 0.1 mol% of Eu^{2+}. The structures, morphologies, chemical compositions, luminescence spectra, lifetimes, quantum yields, and temperature-sensitivity properties were dependent on the annealing temperature. The material contained impurity phases from SrO and $SrCl_2$ when annealed at low temperature (850 °C) and a single phase, ($Sr_3Al_2O_5Cl_2$) at higher annealing temperatures, 1000 and 1200 °C. At the highest annealing temperature (1500 °C), a change of phase to $SrAl_2O_4$ was confirmed from the XRD patterns and the absence of Cl from the EDS spectrum. The luminescence of $Sr_3Al_2O_5Cl_2$:Eu^{2+} was characterized by broad blue and red band emissions and it exhibited complete quenching of the blue band with an increase in the Eu^{2+}-doping concentration and the annealing temperature. In terms of temperature response, the red band showed significant thermal quenching, which was more pronounced in the samples annealed at lower temperatures. Both samples annealed at 850 °C and 1000 °C offer good performance as luminescence thermometers, as the ratio of the temperature-sensitive red band to the temperature-insensitive blue band has a temperature sensitivity well above 1%/°C in the 30 to 100 °C range. This results in the most pronounced colour response among reported phosphors with decay times in the microsecond range, which makes $Sr_3Al_2O_5Cl_2$:Eu^{2+} very well suited for temperature imaging of fast-moving objects, *e.g.*, fluid temperature imaging with a colour camera, *e.g.*, ref. 15.

Author contributions

Hendrik C. Swart: Funding acquisition, supervision, resources and writing – review & editing. Robin E. Kroon: Supervision, resources and writing – review & editing. Frank Beyrau: Resources and writing – review & editing. Christopher Abram and Benoît Fond: Funding acquisition, supervision, conceptualization, investigation, methodology, validation, visualization and writing – review & editing. Simon N. Ogugua: Writing – original draft, conceptualization, investigation, methodology and validation, visualization.

Conflicts of interest

There are no conflicts to declare.

Acknowledgements

South African Research Chairs Initiative of the Department of Science and Technology and the National Research Foundation of South Africa (84415). The World Academy of Science/Deutsche Forschungsgemeinschaft (AB668/1-1). European Commission Marie Curie (708068).

References

1 K. Okabe, N. Inada, C. Gota, Y. Harada, T. Funatsu and S. Uchiyama, *Nat. Commun.*, 2012, **3**, 705.
2 J. P. Feist and A. L. Heyes, *Development of the phosphor thermometry technique for the application in gas turbines,10th international symposium on applications of laser techniques to fluid mechanics*, Lisbon, Portugal, 2000.
3 S. W. Allison and G. T. Gillies, *Rev. Sci. Instrum.*, 1997, **62**, 2615–2650.
4 T. Justel, H. Nikol and C. Ronda, *Angew. Chem., Int. Ed.*, 1998, **37**, 3084–3103.
5 S. Zhang, Y. Nakai, T. Tsuboi, Y. Huang and H. J. Seo, *Chem. Mater.*, 2011, **23**, 1216–1224.
6 R. Zhou, C. Liu, L. Lin, Y. Huang and H. Liang, *Chem. Eng. Sci.*, 2019, **369**, 376–385.
7 C. Abram, I. W. Panjikkaran, S. N. Ogugua and B. Fond, *Opt. Lett.*, 2020, **45**, 3893–3896.
8 C. Abram, B. Fond and F. Beyrau, *Opt. Express*, 2015, **23**, 19453–19468.
9 B. Fond, C. Abram and F. Beyrau, *Appl. Phys. B*, 2015, **121**, 495–509.
10 B. Fond, C. Abram and F. Beyrau, *Opt. Mater.*, 2019, **89**, 615–622.
11 J. Jordan and D. A. Rothamer, *Appl. Phys. B: Lasers Opt.*, 2013, **110**, 285–291.
12 J. Brübach, J. P. Feist and A. Dreizler, *Meas. Sci. Technol.*, 2008, **19**, 025602.
13 I. E. Kolesnikov, A. A. Kalinichev, M. A. Kurochkin, E. V. Golyeva, A. S. Terentyeva, E. Y. Kolesnikov and E. Lähderanta, *Sci. Rep.*, 2019, **9**, 2043.
14 D. Witkowski and D. A. Rothamer, *Proc. Combust. Inst.*, 2019, **37**, 1393–1400.
15 W. Piotrowski, K. Trejgis, K. Maciejewska, K. Ledwa, B. Fond and L. Marciniak, *ACS Appl. Mater. Interfaces*, 2020, **12**, 44039–44048.
16 W. Piotrowski, L. Dalipi, R. Szukiewicz, B. Fond, M. Dramićanin and L. Marciniak, *J. Mater. Chem. C*, 2021, **9**, 12671–12680.
17 D. Dutczak, C. Ronda, A. Meijerink and T. Jüstel, *J. Lumin.*, 2013, **141**, 150–154.
18 R. Chen, Y. Hun, L. Chen, X. Wang, Y. Jin and H. Wu, *Ceram. Int.*, 2014, **40**, 8229–8236.
19 W. Xie, C. Zou, S. Li, J. Sun, F. Kang and G. Sun, *Phys. Chem. Chem. Phys.*, 2018, **20**, 13983–13993.
20 W. Zeng, Y. Wang, Y. Li and X. Xu, *Mater. Res. Soc. Symp. Proc.*, 2014, **1592**, 6466.
21 Z. Wang, Q. Zhang, M. Rong, H. Tan, Q. Wang, Q. Zhou and G. Chen, *Chem. Phys. Lett.*, 2016, **658**, 324–327.
22 Z. Wang, X. Li, L. Xiong, M. Zhou, F. Hu, Y. Zhu and Y. Zhang, *ECS J. Solid State Sci. Technol.*, 2012, **1**, R143–R146.
23 R. D. Shannon, *Acta Crystallogr., Sect. A: Cryst. Phys., Diffr., Theor. Gen. Crystallogr.*, 1976, **32**, 751–767.
24 M. Sato, S. W. Kim, Y. Shimomura, T. Hasegawa, K. Toda and G. Adachi, Rare earth-doped phosphors for white light-emitting diodes, in *Handbook on the physics and chemistry of rare earths*, ed. J.-C. Bünzli and V. K. Pecharsky, Elsevier B.V., 2016, vol. 49, pp. 68–70.
25 L. Ning, C. Zhou, W. Chen, Y. Huang, C. Duan, P. Dorenbos, Y. Tao and H. Liang, *J. Phys. Chem. C*, 2015, **119**, 6785–6792.
26 Y. Lu, X. Li, Y. Dong, Z. Ma, T. Hou, D. Jiao, Q. Guo, L. Guan and F. Teng, *Optik*, 2016, **127**, 4625–4629.
27 A. Vegas, R. L. Martin and D. J. M. Bevan, *Acta Crystallogr., Sect. B: Struct. Sci.*, 2009, **65**, 11–21.
28 D. Dutczak, T. Jüstel, C. Ronda and A. Meijerink, *Phys. Chem. Chem. Phys.*, 2015, **17**, 15236–15249.
29 R. M. Jafer, H. C. Swart, A. Yousif, V. Kumar and E. Coetsee, *J. Lumin.*, 2016, **180**, 198–203.
30 B. M. Jaffar, H. C. Swart, H. A. A. S. Ahmed, A. Yousif and R. E. Kroon, *J. Lumin.*, 2019, **209**, 217–224.
31 H. Tanno, S. Zhang, T. Shinoda and H. Kajiyama, *J. Lumin.*, 2010, **130**, 82–86.
32 Y. Masubuchi, S. Nishitani, A. Hosono, Y. Kitagawa, J. Ueda, S. Tanabe, H. Yamane, M. Higuchi and S. Kikkawa, *J. Mater. Chem. C*, 2018, **6**, 6370–6377.
33 J. S. Kim, Y. H. Park, S. M. Kim, J. C. Choi and H. L. Park, *Solid State Commun.*, 2005, **133**, 445–448.
34 G. Arnaoutakis, *Temperature dependence of phosphors via photo-and thermo- luminescence, Edinburgh Instruments AN_P38*, 2017, DOI: 10.13140/RG.2.2.10709.52967.
35 J. S. Kim, Y. H. Park, J. C. Choi and H. L. Park, *J. Electrochem. Soc.*, 2005, **152**, H135–H137.
36 M. Nazarov, M. G. Brik, D. Spassky and B. Tsukerblat, *J. Lumin.*, 2017, **182**, 79–86.
37 J. Botterman, J. J. Joos and P. F. Smet, *Phys. Rev. B: Condens. Matter Mater. Phys.*, 2014, **90**, 085147.
38 S. N. Ogugua, H. C. Swart and O. M. Ntwaeaborwa, *Sens. Actuators, B*, 2017, **250**, 285–299.
39 M. Takesue, H. Hayashi and R. L. Smith Jr., *J. Prog. Cryst. Growth Charact. Mater.*, 2009, **55**, 98–124.
40 J. El Ghoul and L. El Mir, *J. Mater. Sci.: Mater. Electron.*, 2015, **26**, 3550–3557.
41 J. R. Rubbmark, M. M. Kash, M. G. littman and D. Kleppner, *Phys. Rev. A*, 1981, **23**, 3107–3117.

42 T. Justel, W. Mayr and P. J. Schmidt, Tuning the $4f^15d$-$4f^2$ UV emission of Pr^{3+}, in: 200th meeting of the electrochemical society, San Francisco, CA, USA, 2001.
43 L. G. Van Uitert, *J. Lumin.*, 1984, **29**, 1–9.
44 S. H. M. Poort, W. P. Blocpoel and G. Blasse, *Chem. Mater.*, 1995, **7**, 1547–1551.
45 T. Aitasalo, J. Hölsä, H. Jungner, J.-C. Krupa, M. Lastusaari, J. Legendziewicz and J. Niittykoski, *Radiat. Meas.*, 2004, **38**, 727–730.
46 J. Włodarczyk and B. Kierdaszuk, *Biophys. J.*, 2003, **85**, 589–598.
47 S. N. Ogugua, S. K. K. Shaat, H. C. Swart, R. E. Kroon and O. M. Ntwaeaborwa, *J. Alloys Compd.*, 2019, **775**, 950–968.
48 S. K. Gupta, C. Reghukumar and R. M. Kadam, *RSC Adv.*, 2016, **6**, 53614–53624.
49 C. Cascales, J. Fernández and R. Balda, *Opt. Express*, 2005, **13**, 2141–2152.
50 S. Tombe, G. Adam, H. Heilbrunner, D. H. Apaydin, C. Ulbricht, N. S. Sariciftci, C. J. Arendse, E. Iwuoha and M. C. Scharber, *J. Mater. Chem. C*, 2017, **5**, 1714–1723.
51 J. S. Kim, Y. H. Park, J. C. Choi and H. L. Park, *ESL*, 2005, **8**, H65–H67.
52 J. Ni, Q. Liu, Z. Zhou and G. Liu, *RSC Adv.*, 2017, **7**, 42211–42217.
53 M. Dramićanin, *Luminescence thermometry: methods, materials, and applications*, Woodhead Publ. ser. Electron, 2018, pp. 41–42.
54 B. Cao, Y. Bao, Y. Liu, J. Shang, Z. Zhang, Y. He, Z. Feng and B. Dong, *Chem. Eng. J.*, 2020, **385**, 123906.
55 C. Matuszewska, K. Elzbieciak-Piecka and L. Marciniak, *J. Phys. Chem. C*, 2019, **123**, 18646–18653.
56 R. C. E. Sia, R. A. Arellano-Reyes, T. E. Keyes and J. Guthmuller, *Phys. Chem. Chem. Phys.*, 2021, **23**, 26324–26335.
57 E. J. McLaurin, L. R. Bradshaw and D. R. Gamelin, *Chem. Mater.*, 2013, **25**, 1283–1292.
58 W. Xu, Z. Zhang and W. Cao, *Opt. Lett.*, 2012, **37**, 4865–4867.
59 D. K. Amarasinghe and F. A. Rabuffetti, *Chem. Mater.*, 2019, **31**, 10197–10204.
60 R. Liang, R. Tian, W. Shi, Z. Liu, D. Yan, M. Wei, D. G. Evans and X. Duan, *Chem. Commun.*, 2013, **49**, 969–971.
61 T. P. van Swieten, A. Meijerink and F. T. Rabouw, *ACS Photonics*, 2022, **9**, 1366–1374.
62 M. Suta and A. Meijerink, *Adv. Theory Simul.*, 2020, **3**, 2000176.
63 M. Lawrence, H. Zhao and L. Ganippa, *Opt. Express*, 2013, **21**, 12260–12281.
64 S. Zhou, K. Deng, X. Wei, G. Jiang, C. Duan, Y. Chen and M. Yin, *Opt. Commun.*, 2013, **291**, 138–142.
65 R. F. Zhou, C. M. Liu, L. T. Lin, Y. Huang and H. B. Liang, *Chem. Eng. J.*, 2019, **369**, 376.
66 X. G. Zhang, Z. P. Zhu, Z. Y. Guo, Z. S. Sun and Y. B. Chen, *Chem. Eng. J.*, 2019, **356**, 413–422.
67 B. Chen, C. Li, D. Deng, F. Ruan, M. Wu, L. Wang, Y. Zhu and S. Xu, *J. Alloys Compd.*, 2019, **792**, 702–712.
68 H. Yu, L. Zhou, R. Ye, D. Deng and S. Xu, *Dalton Trans.*, 2022, **51**, 7333–7342.
69 M. Wu, D. Deng, F. Ruan, B. Chen, L. Lei, R. Lei and S. Xu, *Opt. Mater.*, 2019, **88**, 704–710.
70 F. Liu, D. Deng, M. Wu, B. Chen, L. Zhou and S. Xu, *J. Rare Earths*, 2021, **39**, 261–268.
71 R. Zhou, L. Lin, H. Zhao, T. Deng and J. Li, *Mater. Chem. Front.*, 2021, **5**, 6071–6081.
72 C. Wang, H. Lin, X. Xiang, Y. Cheng, Q. Huang, Y. Gao, X. Cui and Y. Wang, *J. Mater. Chem. C*, 2018, **6**, 9964–9971.
73 P. Du, L. Luo, W. Li, F. Yan and G. Xing, *J. Alloys Compd.*, 2020, **826**, 154233.
74 F. Liu, Y. Tian, D. Deng, M. Wu, B. Chen, L. Zhou and S. Xu, *J. Rare Earths*, 2021, **39**, 1311–1319.
75 X. Li, G. Gao, K. Wang, Z. Chen, Z. Gao, Q. Qin, L. Chen and B. Zou, A ratiometric optical thermometer with dual-color emission based on Eu^{2+}-doped $CsCu_2I_3$ microcrystals, *J. Rare Earths*, 2023, DOI: **10.1016/j.jre.2023.07.016**.
76 C. Li, B. Chen, D. Deng, H. Yu, H. Li, C. Shen, L. Wang and S. Xu, *J. Lumin.*, 2020, **221**, 117036.
77 E. I. Kolesnikov, E. V. Afanaseva, M. A. Kurochkin, E. Y. Kolesnikov and E. Lähderanta, *Phys. B*, 2022, **624**, 413456.
78 H. Yu, F. Ruan, L. Chen, D. Deng and D. Deng, *Opt. Mater.*, 2020, **100**, 109678.
79 J. Xue, M. Song, H. M. Noh, S. H. Park, B. C. Choi, J. H. Kim, J. H. Jeong and P. Du, *J. Alloys Compd.*, 2020, **843**, 155858.
80 T. Yu, B. Liu, Z. Ma, Y. Jiang, Q. Zeng, D. Wen and Y. Guo, *Mater. Chem. Front.*, 2021, **5**, 6256–6264.
81 T. Hu, Y. Gao, M. Molokeev, Z. Xia and Q. Zhang, *Sci. China Mater.*, 2019, **62**, 1807–1814.
82 C. Li, B. Chen, D. Deng, M. Wu, H. Yu, H. Li, C. Shen, L. Wang and S. Xu, *J. Alloys Compd.*, 2020, **838**, 155675.
83 A. Mendieta, B. Fond, P. Dragomirov and F. Beyrau, *Meas. Sci. Technol.*, 2019, **30**, 074002.